Identification of Jupiter's magnetic equator through H3+ ionospheric emission

Article

Accepted Version

Identification of Jupiter's magnetic equator within H_3^+ ionospheric emission

Authors: Tom S. Stallard[1*], Angeline G. Burrell[1,2], Henrik Melin[1], Leigh N. Fletcher[1], Steve Miller[3], Luke Moore[4], James O'Donoghue[5], John E. P. Connerney[5], Takehiko Satoh[6], Rosie E. Johnson[1]

Affiliations:

[1]Department of Physics and Astronomy, University of Leicester, University Road, Leicester LE1 7RH, U.K.

[2]Department of Physics, University of Texas at Dallas, 800 West Campbell Road, Richardson, TX 75080, U.S.A.

[3]Department of Physics and Astronomy, University College London, Gower Street, London WC1E 6BT, U.K.

[4]Center for Space Physics, Boston University, *725* Commonwealth Avenue*,* Room 506*,* Boston, MA 02215, USA

[5]Goddard Space Flight Center, NASA, Mail Code: 695, Greenbelt, MD 20771

[6]Institute of Space and Astronautical Science, JAXA, Yoshinodai 3-1-1, Chuo-ku, Sagamihara, Kanagawa, 252-5210, Japan

May 31, 2018

Abstract:

Our understanding of Jupiter's magnetic field has been developed through a combination of spacecraft measurements at distances >1.8 R_J and images of the aurora (*1–7*). These models all agree on the strength and direction of the jovian dipole magnetic moments, but, because higher order magnetic moments decay more strongly with distance from the planet, past spacecraft measurements could not easily resolve them. In the past two years, the Juno mission has measured very close to the planet (>1.05 R_J), observing a strongly enhanced localized magnetic field in some orbits (*8-9*) and resulting in models that identify strong hemispheric asymmetries at mid-to-high latitudes (10, 11). These features could be better resolved by identifying changes in ionospheric density caused by interactions with the magnetic field, but past observations have been unable to spatially resolve such features (*12–14*). In this study, we identify a dark sinusoidal ribbon of weakened H_3^+ emission near the jovigraphic equator, which we show to be an ionospheric signature of Jupiter's magnetic equator. We also observe complex structures in Jupiter's mid-latitude ionosphere, including one dark spot that is coincident with a localized enhancement in Jupiter's radial magnetic field observed recently by Juno (*10*). These features reveal evidence of complex localized interactions between Jupiter's ionosphere and its magnetic field. Our results provide ground-truth for Juno spacecraft observations and future ionospheric and magnetic field models.

The NASA InfraRed Telescope Facility observed Jupiter over a period of 48 nights between 1995-2000, using the NSFCam instrument (*15*) to take images at wavelengths of 3.42-3.46 and 3.53 microns in order to measure emission from the ionic molecule H_3^+, a dominant ion in Jupiter's upper atmosphere. These filters include light from the lower atmosphere that cannot be removed from individual images, preventing an accurate measure of ionospheric emission. Here, instead of measuring the ionosphere on an individual night, we produce a measure of the mean H_3^+ ionospheric emission over a period of several years. Any magnetically induced density changes will consistently appear at the same SIII latitude and longitude and, since Jupiter's upper atmosphere broadly co-rotates with the magnetic field (*16*), any magnetically forced temperature differences will also be broadly fixed in SIII (*17*). Jupiter's troposphere, however, rotates at a different rate to the magnetic field, and so it is possible to isolate ionospheric density differences caused by the magnetic field by observing the ionosphere over an extended period of at least several months, so that the rotational phase of the underlying neutral atmosphere is completely de-coupled from the SIII longitudinal system (*18*). If tropospheric weather features move with a velocity of order 100 m/s in SIII, in ~50 days these features would complete one full rotation around the planet. Equatorial observations are further complicated by the recent discovery that ionospheric emissions are enhanced above the Great Red Spot (*19*), through an as-yet unknown process, but such processes are again coupled to Jupiter's lower atmosphere. This means that brightness changes associated with the underlying troposphere can be removed from the average image brightness observed over five years, using a process described in the Methods section, resulting in a map that highlights any spatial differences in Jupiter's H_3^+ emission, completely de-coupled from the troposphere.

This map, shown in Figure 1, reveals both large- and small-scale non-auroral emission structures. Since H_3^+ brightness is driven by both H_3^+ density (which controls the emission through the number of emitting molecules per unit volume) and thermosphere temperature (which determines the energy emitted per H_3^+ molecule), and since the image filter includes emission from multiple lines of H_3^+, we cannot measure absolute line brightness. Instead we compare the brightness of features with the brightest auroral feature observed across all longitudes between 75˚N and 75˚S, designated here as the peak Main Auroral Brightness (MAB). The measured average brightness between 35˚N and 35˚S is 7.34% MAB.

At the largest scales, there are two ionospheric regions that appear darker: a longitude band between about 30˚-150˚W with localized patches of darkness, concentrated in the northern hemisphere, where emission drops as low as 5.5% MAB; and a region of weaker darkening at longitudes between 180˚-270˚W, extending across the southern hemisphere and as far as ~10˚N, where emissions are ~6.5-7% MAB. These two darker regions are surrounded by brighter regions where emissions are >7.5% MAB. The first of these darker regions has previously been identified, but at spatial scales too large to resolve any of the small-scale features we observe here (*13, 14*). This region is co-incident with a region of enhanced neutral atmospheric emission named the 'Lyman-α bulge' that has previously been inferred to be associated with the decrease in the H_3^+ density through electron recombination (*20*). No Lyman-α observations have been obtained at the spatial resolution required to identify small-scale structures.

One of the most prominent small-scale ionospheric features is a darkened 'ribbon' of weak emission that appears to undulate with an approximately sinusoidal form within about 15˚ of the jovigraphic equator, roughly following the path of the northern and southern auroral oval limits. This ribbon has its lowest intensity at 20˚N, 90˚W and 15˚S, 220˚W, where emission drops as low as 5.5% MAB, but forms a continuing narrow ribbon of lowered emission across most longitudes. This feature is observed in each of the H_3^+ filters used in the study, as shown in the supplemental information.

Past ionospheric modelling has suggested that localized equatorial H_3^+ densities should be directly affected by Jupiter's magnetic field (21). Photoelectrons, electrons produced through the photoionization of a neutral particle, play an important role in the creation of H_3^+. In the jovian upper atmosphere, collisions between photoelectrons and H_2 are a significant source of H_3^+. Because photoelectrons preferentially travel along magnetic field lines, the horizontal orientation of the field lines at the magnetic equator diverts photoelectrons to higher latitudes as they move to lower altitudes. This mechanism thus reduces the H_3^+ column production rate in the vicinity of the magnetic equator. Current modelling is too spatially coarse to fully resolve this effect, but suggests that the corresponding H_3^+ density is reduced by at least 1-2% within ~10˚ of the jovimagnetic equator (*21*).

The observed H_3^+ emission in this region is consistent with this process, although the observed reduction in brightness is larger than predicted. Deflected photoelectrons should also slightly enhance the photoelectron density immediately poleward of the magnetic equator, potentially explaining the small enhancement in H_3^+ emission in this region. Since the sinusoidal morphology of the darkened ribbon is difficult to

explain as a stable thermospheric cooling structure, the dark ribbon is most likely caused by a reduction in the local H_3^+ density, strongly suggesting that it demarcates the location of the jovimagnetic equator. We considered the possibility that the dark ribbon and flanking features were caused by an alternative ionospheric process, such as the 'fountain effect' similar to that which produces Earth's Equatorial Ionization Anomaly (*22*). However, this transport-driven process only shapes the terrestrial F region and does not influence lower altitude layers that are dominated by chemistry. Since the H_3^+ emission peak at Jupiter is in photochemical equilibrium (*21*), it is improbable that the H_3^+ density depletion is shaped by a similar fountain process.

To find the position of the dark ribbon, we averaged the emission intensity over 10˚ longitudinal bins between 20˚N and 20˚S, fitting the selected data with a negative Gaussian profile of brightness as a function of latitude. These positions are identified in the bottom-left panel of Figure 1 (yellow crosses) and are listed in Table 1. We then averaged the H_3^+ emission across all longitudes against distance from the dark ribbon and plotted this average emission against distance (shown in the bottom right panel of Figure 1). This latitudinal profile has a significant decrease of ~0.8% MAB at its centre (~12% of the non-auroral brightness) and increases with latitude on either side of the dark ribbon, such that the mean non-auroral level of emission is attained at locations about 10˚ away from the centre. This is surrounded by a slight, localized brightening of ~0.1% MAB (~1.5% of the non-auroral brightness) 20˚ either side of the dark ribbon's centre.

Further support for the dark ribbon marking the location of the jovimagnetic equator comes from the observed location of the jovian H Lyman-α bulge, theorised to be

offset from the jovigraphic equator as a result of magnetic field distortions (*20*). The calculated peak UV emission latitudes, shown in Figure 2 by the blue-dashed line, overlaps with the location of the dark ribbon within the errors of both measurements.

As discussed previously, the recently published JRM09 model (11) now provides a 10 degree spherical harmonic model of Jupiter's magnetic field. In Figure 2 we compare the smoothed location of the dark ribbon with the modelled magnetic particle drift equator calculated from the JRM09 model. The inferred magnetic equator follows the modelled magnetic equator very closely across most longitudes and is typically located within ±5˚ of the spacecraft derived magnetic equator. The only location where the magnetic field is not co-located is in the 0-60˚W range, where the darkening at the equator is particularly weak. The close alignment of the dark ribbon and the JRM09 equator strongly suggests that the dark ribbon is an ionospheric feature that is directly associated with the magnetic field lines that uniquely run parallel to the surface at Jupiter's magnetic equator. It also suggests that the location of Jupiter's magnetic equator has remained stable over the over the 15 years separating these two independent measurements.

Away from the equatorial regions, our observations show significant local brightness changes. In the 60-140˚W region we observe a longitudinally broad darkening (5.5% MAB) at ~40˚N (poleward of the dark ribbon) and a narrow dark spot (6% MAB) focused on 25˚S, 90˚W. In addition, two dark arcs (7% MAB) are visible at 25˚-40˚N and ~60˚N between 270˚ and 330˚W, within a broad region of raised emission (about 8-10% MAB).

171 These localized dark regions could result from either lower ion density or a localized
172 region of cooling. The most poleward arc, at ~60˚N and around 300˚W was recently
173 identified as a 'Great Cold Spot' in Jupiter's thermosphere, where local temperatures
174 are ~150 K cooler than the surroundings (*17*). None of the other features identified
175 here have previously been observed.
176
177 While a detailed modelling of Jupiter's magnetic field awaits more orbits from Juno,
178 magnetic measurements from the first perijove pass (PJ1) revealed that Jupiter's
179 radial field appears to be enhanced by a factor of two on field lines that map to 30-
180 45˚N and 90˚W (*10*). This region is directly aligned with the strongest darkening in
181 our ionospheric emission maps. If future spectral observations reveal that this dark
182 region is caused by decreased density, this strongly suggests lower precipitating
183 electron flux from the magnetosphere in this region, due to the localized enhancement
184 in the magnetic field strength; this would be the inverse of the enhanced ionosphere
185 observed in Earth's South Atlantic anomaly, where the magnetic field strength is a
186 local minimum.
187
188 Detailed ionospheric modelling, combined with follow-up spectral observations, will
189 allow us to test what ionospheric process drives the darkening of H_3^+ at Jupiter's
190 jovimagnetic particle drift equator, providing us with new insights into Jupiter's
191 equatorial ionosphere. The continuing magnetic measurements made by Juno will
192 allow us to further assess whether or not the mid-latitude localized dark regions are
193 driven by Jupiter's localized magnetic structure. If this is the case, we have
194 discovered an alternative measure of Jupiter's magnetic field at a comparable spatial
195 scale to the longitudinal gaps between the planned orbits of Juno, providing a ground-

196 truth for the Juno magnetometer dataset. With a two-decade gap in observation and
197 the potential for ongoing monitoring into the future, this may allow us to reveal the
198 rate of change in Jupiter's complex mid-latitude magnetic field, thus providing new
199 insight into Jupiter's internal processes.
200

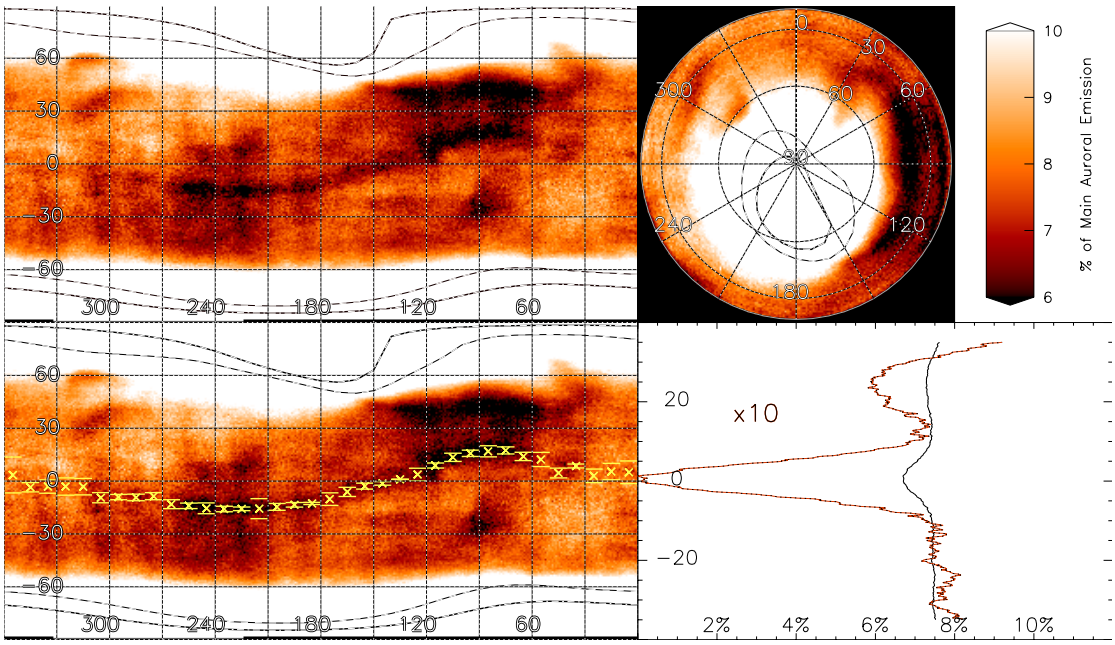

201

202 Figure 1: H_3^+ ionospheric emission at wavelengths of 3.42-3.46 and 3.53 micron. The
203 top-left panel shows a cylindrical map of the square root of the MAB-scaled equatorial
204 H_3^+ emission (see text), scaled between 6% and 10% of MAB, and the top-right panel
205 shows the same map in northern polar orthographic projection. The location of the main
206 auroral emission (black and white dot-dashed line) and Io spot and trail (black and white
207 dashed line) are taken from the Grodent et al (2008) model. The bottom-left panel
208 shows the same map, overlain by the calculated positions of the dark ribbon from Table
209 1 (yellow-crosses), bounded by the standard-deviation error of these fitted positions
210 (yellow lines). The bottom-right panel shows the latitudinal profile of emission 35°
211 either side of the fitted dark ribbon position averaged over all longitudes (black line).
212 This is also shown scaled by a factor of 10, for clarity (red).

213 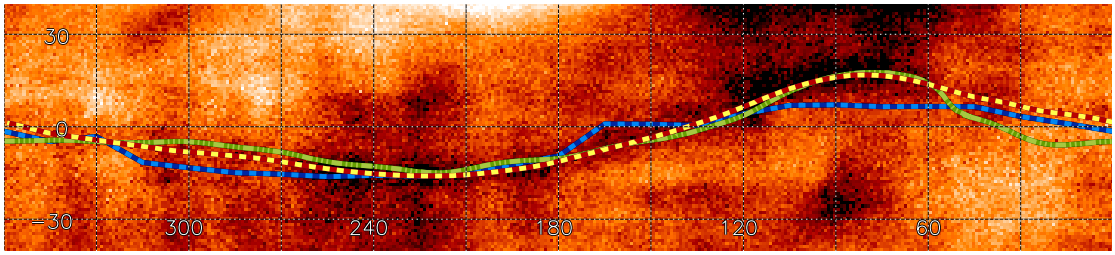

214 Figure 2: Equatorial magnetic field mapping. Here, we show the same cylindrical map
215 of equatorial H_3^+ emission in Figure 1, with the same scaling, from 40˚N to 40˚S.
216 Overlain on this are: a rolling 13-element cubic fit of the dark ribbon positions (red-
217 yellow dashed line); the central positions of the UV H Ly-α emission (*20*; blue dashed
218 line); and the JRM09 magnetic field model particle drift equator, where the magnetic
219 field lines are parallel to Jupiter's 'surface' (*11*; light green four-dash line).

220

West longitude (degrees)	Latitude (degrees)	Latitude error (degrees)
0-10	5.0	6.5
10-20	5.4	4.6
20-30	3.0	4.2
30-40	8.6	1.0
40-50	4.6	3.0
50-60	12.3	4.2
60-70	14.0	2.0
70-80	17.4	1.4
80-90	16.9	2.8
90-100	15.8	1.5
100-110	13.5	2.5
110-120	8.8	0.9
120-130	4.6	3.3
130-140	1.0	0.2
140-150	-1.3	1.4
150-160	-2.9	1.4
160-170	-6.2	2.7
170-180	-10.2	2.9
180-190	-12.7	0.3
190-200	-13.5	1.3
200-210	-14.7	1.0
210-220	-15.7	6.3
220-230	-15.8	1.2
230-240	-15.8	1.5
240-250	-15.5	2.9
250-260	-14.1	1.6
260-270	-13.1	3.0
270-280	-8.6	1.7
280-290	-9.3	1.5
290-300	-9.1	1.3
300-310	-9.5	3.0

310-320	-3.2	4.1
320-330	-3.1	4.4
330-340	-3.1	3.9
340-350	-3.5	2.7
350-360	3.4	10.1

221

222 Table 1: The calculated position of the dark ribbon (a proxy for the jovian magnetic
223 equator). The latitudes shown were calculated by binning emission between 20˚N and
224 20˚S in 10-degree longitude bins and fitting a minimum Gaussian peak.

225

226

227 **References**

228 (*1*) Smith, E. J., Davis, L., Jr., Jones, D. E., Coleman, P. J., Jr., Colburn, D. S., Dyal,
229 P., Sonett, C. P., & Frandsen, A. M. A., The planetary magnetic field and
230 magnetosphere of Jupiter: Pioneer 10. *J. Geophys. Res.* **79**, 3501, DOI:
231 10.1029/JA079i025p03501 (1974).

232 (2) Smith, E. J., Davis, L., Jr., Jones, D. E., Coleman, P. J., Jr., Colburn, D. S., Dyal,
233 P., & Sonett, C. P. Jupiter's magnetic field, magnetosphere, and interaction with the
234 solar wind - Pioneer 11. *Science* **188**, 451-455, DOI: 10.1126/science.188.4187.451
235 (1975)

236 (3) Connerney, J. E. P. The magnetic field of Jupiter - A generalized inverse
237 approach. *J. Geophys. Res.* **86**, 7679-7693, DOI:10.1029/JA086iA09p07679 (1981)

238 (*4*) Connerney, J. E. P., Acuña, M. H., Ness, N. F., Satoh, T. New models of Jupiter's
239 magnetic field constrained by the Io flux tube footprint. *J. Geophys. Res.* **103**,
240 11929-11940, DOI:10.1029/97JA03726 (1998)

(*5*) Connerney, J.E.P., Volume 10: Planets and Satellites, in Treatise in Geophysics, eds. G. Schubert, T. Spohn, Elsevier, Oxford, UK, 2007

(*6*) Grodent, D., Bonfond, B., Gérard, J.-C., Radioti, A., Gustin, J., Clarke, J. T., Nichols, J., Connerney, J. E. P. Auroral evidence of a localized magnetic anomaly in Jupiter's northern hemisphere. *J. Geophys. Res.* **113**, A09201- DOI:10.1029/2008JA013185 (2008)

(*7*) Hess, S. L. G., Bonfond, B., Zarka, P., Grodent, D. Model of the Jovian magnetic field topology constrained by the Io auroral emissions. *J. Geophys. Res.* **116**, A05217- DOI:10.1029/2010JA016262 (2011)

(*8*) Bolton, S. J., Adriani, A., Adumitroaie, V., Allison, M., Anderson, J., Atreya, S., Bloxham, J., Brown, S., Connerney, J. E. P., DeJong, E., Folkner, W., Gautier, D., Grassi, D., Gulkis, S., Guillot, T., Hansen, C., Hubbard, W. B., Iess, L., Ingersoll, A., Janssen, M., Jorgensen, J., Kaspi, Y., Levin, S. M., Li, C., Lunine, J., Miguel, Y., Mura, A., Orton, G., Owen, T., Ravine, M., Smith, E., Steffes, P., Stone, E., Stevenson, D., Thorne, R., Waite, J., Durante, D., Ebert, R. W., Greathouse, T. K., Hue, V., Parisi, M., Szalay, J. R., Wilson, R. Jupiter's interior and deep atmosphere: The initial pole-to-pole passes with the Juno spacecraft. *Science* **356**, 821-825, DOI:10.1126/science.aal2108 (2017)

(*9*) Connerney, J. E. P., Adriani, A., Allegrini, F., Bagenal, F., Bolton, S. J., Bonfond, B., Cowley, S. W. H., Gerard, J.-C., Gladstone, G. R., Grodent, D., Hospodarsky, G., Jorgensen, J. L., Kurth, W. S., Levin, S. M., Mauk, B., McComas, D. J., Mura, A., Paranicas, C., Smith, E. J., Thorne, R. M., Valek, P., Waite, J. Jupiter's magnetosphere and aurorae observed by the Juno spacecraft during its first polar orbits. *Science* **356**, 826-832, DOI:10.1126/science.aam5928 (2017)

(10) Moore, K. M., Bloxham, J., Connerney, J. E. P., Jørgensen, J. L., Merayo, J. M. G. The analysis of initial Juno magnetometer data using a sparse magnetic field representation. *Geophys. Res. Lett.* 44, 4687-4693, DOI:10.1002/2017GL073133 (2017)

(11) Connerney, J. E. P., Kotsiaros, S., Oliversen, R. J., Espley, J. R., Joergensen, J. L., Joergensen, P. S., et al. (2018). A new model of Jupiter's magnetic field from Juno's first nine orbits. *Geophys. Res. Lett.* **45**. DOI: 10.1002/2018GL077312

(*12*) Stallard, T. S., Melin, H., Miller, S., Badman, S. V., Baines, K. H., Brown, R. H., Blake, J. S. D., O'Donoghue, J., Johnson, R. E., Bools, B., Pilkington, N. M., East, O. T. L., Fletcher, M. Cassini VIMS observations of H_3^+ emission on the nightside of Jupiter. *J. Geophys. Res.* **120**, 6948-6973, DOI:10.1002/2015JA021097 (2015)

(*13*) Lam, H. A., Achilleos, N., Miller, S., Tennyson, J., Trafton, L. M., Geballe, T. R., Ballester, G. E. A Baseline Spectroscopic Study of the Infrared Auroras of Jupiter. *Icarus* **127**, 379-393, DOI:10.1006/icar.1997.5698 (1997)

(*14*) Miller, S., Achilleos, N., Ballester, G. E., Lam, H. A., Tennyson, J., Geballe, T. R., Trafton, L. M. Mid-to-Low Latitude H_3^+ Emission from Jupiter. *Icarus* **130**, 57-67, DOI:10.1006/icar.1997.5813 (1997)

(*15*) Shure, M. A., Toomey, D. W., Rayner, J. T., Onaka, P. M., Denault, A. J. NSFCAM: a new infrared array camera for the NASA Infrared Telescope Facility. *Instrumentation in Astronomy VIII* **2198**, 614-622, DOI:10.1117/12.176769 (1994)

(*16*) Johnson, R. E., Stallard, T. S., Melin, H., Miller, S., Nichols, J. D. Measurements of the rotation rate of the jovian mid-to-low latitude ionosphere. *Icarus* **280**, 249-254, DOI:10.1016/j.icarus.2016.06.026 (2016)

(*17*) Stallard, T. S., Melin, H., Miller, S., Moore, L., O'Donoghue, J., Connerney, J. E. P., Satoh, T., West, R. A., Thayer, J. P., Hsu, V. W., Johnson, R. E. The Great Cold Spot in Jupiter's upper atmosphere. *Geophys. Res. Lett.* **44**, 3000-3008, DOI:10.1002/2016GL071956 (2017)

(*18*) Fletcher, L. N., Greathouse, T. K., Orton, G. S., Sinclair, J. A., Giles, R. S., Irwin, P. G. J., Encrenaz, T. Mid-infrared mapping of Jupiter's temperatures, aerosol opacity and chemical distributions with IRTF/TEXES. *Icarus* **278**, 128-161, DOI:10.1016/j.icarus.2016.06.008 (2016)

(*19*) O'Donoghue, J., Moore, L., Stallard, T. S., Melin, H. Heating of Jupiter's uppeghjghjghjghjghjghjghjghjgjghjr atmosphere above the Great Red Spot. *Nature* **536**, 190-192, DOI:10.1038/nature18940 (2016)

(*20*) Melin, H., Stallard, T. S. Jupiter's hydrogen bulge: A Cassini perspective. *Icarus* **278**, 238-247, DOI:10.1016/j.icarus.2016.06.023 (2016)

(*21*) Achilleos, N., Miller, S., Tennyson, J., Aylward, A. D., Mueller-Wodarg, I., Rees, D. JIM: A time-dependent, three-dimensional model of Jupiter's thermosphere and ionosphere. *J. Geophys. Res.* **103**, 20089-20112, DOI:10.1029/98JE00947 (1998)

(*22*) Hanson, W. B., Moffett, R. J. Ionization transport effects in the equatorial F region. *J. Geophys. Res.* **71**, 5559-5572, DOI:10.1029/JZ071i023p05559 (1966)

Correspondence to: Tom Stallard at tss8@leicester.ac.uk

Acknowledgements:

This work was supported by the UK STFC Consolidated grant ST/N000749/1 for H. Melin and T. Stallard and a PhD studentship for R. Johnson. A.G. Burrell was supported by NERC Grant NE/K011766/1 and the start-up funds provided to R. Stoneback by the University of Texas at Dallas. Fletcher was supported by a Royal Society Research Fellowship at the University of Leicester. L.M. was supported by NASA under Grant NNX17AF14G issued through the SSO Planetary Astronomy Program. J.E.P. Connerney and T. Satoh were visiting astronomers at the NASA Infrared Telescope Facility, which is operated by the University of Hawaii under Cooperative Agreement no. NNX-08AE38A with the National Aeronautics and Space Administration, Science Mission Directorate, Planetary Astronomy Program. Infrared images from 1995-2000 are available from the Magnetospheres of the Outer Planets Infrared Data Archive.

Individual contributions:

T.S.S. Project leader, data reduction, data analysis, figure production, paper writing

A.G.B. Equatorial modelling for Earth comparison, detailed discussions, writing for magnetic field interactions, general corrections

H.M. Data analysis: image processing and limb fitting techniques, general corrections

L.N.F. Data analysis: tropospheric emission, discussion of troposphere, general corrections

S.M. Discussion of data analysis techniques, general corrections

L.M. Detailed discussions of Jupiter's ionosphere, writing for ionosphere, general corrections

J.O. Discussion of ionospheric darkening, general corrections

J.E.P.C. Project leader on original observations, data reduction, detailed discussions of magnetic field modelling, general corrections

T.S. Observer, detailed discussion of instrumental errors, lead discussion on testing of image processing technique, general corrections

R.E.J. Discussion of data analysis techniques, general corrections

Methods

Introduction

This study uses 13,501 images of H_3^+ emission taken over 48 nights between 1995 and 2000 (*23*). These images were taken using the NSFCam instrument at the NASA InfraRed Telescope Facility (15) using a range of filters that cover the 3.4-3.6 micron range, starting from the sky-subtracted and flat-fielded images produced for the 'Magnetospheres of the Outer Planets Infrared Data Archive'. These observations are described in detail within the supplementary information of Stallard et al., 2017 (17), along with a full description of the initial reduction technique used for these images. Here, we briefly describe these techniques and then detail the additional techniques that are unique to this paper.

The 'Magnetospheres of the Outer Planets Infrared Data Archive' provides two kinds of image, individual flat-fielded and sky subtracted images and 'reduced' combined data, where individual images have been stacked together. In order to properly

355 remove bad data and provide an accurate limb fit, we use the former individual
356 images.

357 These images consist of a range of different wavelength settings, focused on
358 wavelengths with H_3^+ emission, with earlier observations using the NSFCam CVF
359 centered on three different wavelengths, 3.420, 3.430 and 3.460 micron, with a
360 spectral resolution of ~50 and later images utilizing two very narrow fixed filters with
361 a central wavelength of 3.4265 and 3.542 micron and a spectral resolution of 200. The
362 precise filter distributions for each of these settings is not well known, so we are
363 unable to produce precise values for H_3^+ line intensity. Instead, we measure the peak
364 auroral brightness between 75˚N and 75˚S (avoiding the poles to remove errors in
365 line-of-sight correction) for each individual filter and use this to scale the non-auroral
366 filter emission.

367 Internal reflections within the NSFCam imager cause a rotated and reversed image to
368 appear within the data as a 'ghost'. The brightness of this ghost varies significantly,
369 depending upon unknown factors, most likely instrument illumination angles. This
370 results in a 'ghost' image with a brightness of 0.001-0.05 of the primary signal. As a
371 result, subtracting the signal is difficult, and instead, we mask this signal out
372 completely, removing a region of the image brighter than our threshold, set to 17.5 in
373 our raw data (before main auroral brightening is scaled for), as well as +/- 40 pixels in
374 both x and y around the center of any bright moon within the image. This results in a
375 blanked out region within each region, which can be seen in Supplementary Figure 1
376 as two black regions (a square in one corner and a curved image) at the bottom of the
377 image. Data in this region is ignored in our mapping. Again, this process is described

in more detail in the supplementary information for Stallard et al., 2017 (17), and is tested within the supplementary information for this paper.

We then fit the center of the planet within each image using a by-eye limb fitting technique. We estimate that this resulted in a positional accuracy of <0.5". In Stallard et al., 2017 (17), this planetary center is used to calculate the latitude and longitude for each corner of each pixel within each image that transects the planetary disk, and use this to map the data into a latitude and longitude grid, allowing us to combine every image into an average brightness map. We apply the same mapping here, but before mapping the data, we apply a line-of-sight correction, to correct for limb brightened H_3^+.

Line-of-sight correction to images

The H_3^+ emission measured within an image is geometrically enhanced as a function of the apparent geometric position on the planetary disk, increasing towards the limb of the planet as a result of an increased depth of the radiating column of H_3^+ observed. This geometric effect distorts emission from across the entire disk of the planet, but is clearest on the equatorial limb, since H_3^+ emission in this region is uniformly generated by solar ionisation, yet the apparent brightness increases at the limb. Supplementary Figure 1a shows a clear limb enhancement within the auroral region, where the apparently brightest aurora is incident with the limb, with the non-auroral ionospheric emission also showing enhancement along the dusk limb down to equatorial regions.

We calculate a theoretical enhancement for the planetary geometry of each individual image, as shown in Supplementary Figure 1b-i. The center of the planet has been fitted for each image by-eye. Accounting for the equatorial diameter of the planet, the flattening of Jupiter, and the sub-Earth latitude, this provides a ratio of the radial distance of each pixel (r_x), relative to both the center of the planet and the 1 bar limb (r_1). We then model emission as a uniform shell of emission 100km thick, positioned at altitude of 400km (r_2) and 500km (r_3) above the 1 bar surface (r_1). We model the atmosphere as opaque below this 1 bar limb and transparent above it.

The enhancement is thus calculated as the geometric enhancement of emission compared with the geometric center of the planet:

Below the limb ($r_x < r_1$): $\sqrt{r_3^2 - r_x^2}$ - $\sqrt{r_2^2 - r_x^2}$

Below the H_3^+ layer ($r_1 < r_x < r_2$): $2\left[\sqrt{r_3^2 - r_x^2} - \sqrt{r_2^2 - r_x^2}\right)\right]$

Within the H_3^+ layer ($r_2 < r_x < r_3$): $2\sqrt{r_3^2 - r_x^2}$

This gives the idealised H_3^+ enhancement for any position within the image, but since we are observing Jupiter from Earth, the distorting effect of turbulence within Earth's atmosphere, the 'seeing', will blur out this line-of-sight enhancement.

We have calculated the mean seeing for each night using star calibration images taken on each night. We fit each individual star image with a Gaussian in four directions, 0°-180°, 45°-225°, 90-270° and 135-315° to produce an average full-width half-maximum (FWHM) for each star image. The mean seeing is the average FWHM

across all the star images for each night. These are listed for each night in Stallard et al. (2017).

In order to calculate the seeing-convolved line-of-sight enhancement, we take the theoretical line-of-sight enhancement and convolve this using a 2D Gaussian with a FWHM of the nightly seeing. This results in a more realistic line-of-sight enhancement with which to correct our image, shown in Supplementary Figure 1b-ii, scaled to ensure that the correction at the geometric center of the planet is at unity. This more realistic line-of-sight enhancement is used to correct our data: dividing the image by this seeing-convolved line-of-sight converts the line-of-sight brightness to a vertical column-integrated, as shown in Supplementary Figure 1c.

Removal of thermospheric emission

Once the images have been mapped, we can measure the resultant time-averaged image brightness from Jupiter, shown in Supplementary Figure 2. This image still contains the longitudinally smoothed reflected sunlight from the troposphere and can be directly compared with the Figure 1 of the paper, which shows the same emission once this tropospheric background has been removed. Because the image filter settings used obscure the exact spectral characteristics of the H_3^+ emission that dominates these images, we normalise the brightness of our maps to the brightest auroral emission equatorward of 75°. We refer to this emission level in the paper as the main auroral brightness (MAB). The top row of Supplementary Figure 2 shows a cylindrical projection of H_3^+ emission alongside an orthographic polar projection, which shows the northern auroral region.

The bottom rows of Supplementary Figure 2 show this same cylindrical map in the first column, now scaled to enhance the non-auroral emission by scaling the emission intensity between 10% MAB and below 6% MAB, again with the color scale stretched by the square root. At this intensity level, the non-auroral intensity appears to be dominated by two bright bars that stretch across all longitudes at about 8˚N and 18˚S. This emission does not coincide with ionospheric features in past spectral observations, but instead coincides approximately with observations of Jupiter's tropospheric emission (18), typically observed at longer wavelengths (*e.g.* 5.32 microns). The exact locations of tropospheric bands vary significantly with wavelength, and tropospheric emission has not previously been measured at wavelengths as short as ~3.5 microns, so we cannot be sure of what are the expected morphology of these tropospheric regions, but the approximate location of the two bands is similar to that observed at 5 microns, as shown in the bottom right panel of Supplementary Figure 3. This emission appears to escape absorption in the stratosphere through narrow absorption gaps at about 3.44 and 3.52 microns, identified in standard Jupiter spectra taken from the IRTF spectral library (*24*).

Although tropospheric emissions are localized, they are also highly dynamic. Since the troposphere is generally fixed within Jupiter's System I and II coordinates, the emissions from these atmospheric storms and spots will have completely smeared out over the six-year period in the System III coordinates used to create this emission map, resulting in a longitudinally uniform tropospheric contribution that would not be significant in emission maps from a single night. In order to remove this non-ionospheric signal, we measure the longitudinally averaged map brightness, shown in

476 the bottom right panel of Supplementary Figure 2. We cannot be sure of the total
477 brightness of this tropospheric contribution, but typical measures of this emission at
478 other wavelengths (shown as the red dashed line) suggest that they are brightest at the
479 equator, and are typically much weaker and smooth between 28˚-35˚N and 25˚-35˚S.
480 Thus, we use these regions poleward of the equator (shown in blue in the bottom-right
481 panel) to model the background emission (which consists of both tropospheric and
482 ionospheric emission) a second-order polynomial (shown by the blue dashed line).
483 Subtracting this background from the longitudinally averaged intensity profile
484 provides us with a model of the longitudinally-smoothed tropospheric intensity.
485
486 The tropospheric background intensity model is not calibrated in absolute brightness,
487 but does make it possible to produce a map of the relative brightness of H_3^+ emissions.
488 Because the tropospheric signal is longitudinally smoothed over the 48 nights of
489 observation while most H_3^+ emission structure is fixed to the magnetic field, only H_3^+
490 features that are associated with non-System III coordinates, such as the recent
491 detection of bright H_3^+ emission associated with the Great Red Spot (19), will be lost
492 through this technique. It is also possible that the H_3^+ emission brightness in the
493 equatorial region has been over-estimated, due to an under-estimation of the
494 tropospheric brightness – however, the location of ionospheric features (revealed by
495 relative brightening and darkening) is well defined by this method.
496

497 **Identifying the location of the equatorial dark ribbon**

498 In order to measure the location of the dark ribbon that appears to follow Jupiter's
499 magnetic equator, shown in Figure 1 of the paper, we fitted latitudinal profiles of the
500 data, binned in longitude, with negative Gaussians. Firstly, we took the emission

between 20N and 20S and binned it into 10˚ longitude bins. This resulted in 36 latitudinal profiles, shown in Supplementary Figure 3. We provided an initial estimated depth and location of the dark ribbon, in order to provide the fitting procedure with a starting Gaussian shape, then fitted each profile with a Gaussian and quadratic background – if the resultant fit produced a positive value, or a central position outside 20˚N and 20˚S, the values for the starting Gaussian shape were randomly changed until a fit within these constraints was found (this removed some instances where the Gaussian fitting procedure assumes the entire profile is part of the flank of the Gaussian, resulting in nonsensical dark ribbon positions). This fit provided an assessment of the noise level of the data once the Gaussian was accounted for. We then tested the errors in this fitted position by obtaining the calculated noise level from the original fit, and randomly regenerating the noise in the data, and refitting the data, a process that we repeated 1000 times. The standard deviation in the fitted positions across these 1000 fits was then calculated, to provide a measurement of the fitting error. The Gaussian position and fitting errors are described in Table 1 of the paper and are shown as yellow crosses and lines in the bottom panel of Figure 1 in the paper.

Additional Methods References

(*23*) Stallard, Tom, 2018, "The Magnetospheres of the Outer Planets Infrared Data Archive: IRTF NSFCAM 1995-2000", https://doi.org/10.7910/DVN/KVQWNJ, Harvard Dataverse, V1

(*24*) Rayner, J. T., Cushing, M. C., Vacca, W. D. The Infrared Telescope Facility (IRTF) Spectral Library: Cool Stars, *The Astrophysical Journal Supplement Series* **185**, 289-432, DOI:10.1088/0067-0049/185/2/289 (2009),

Data Availability Statement

The data used in this study was originally released as the Magnetospheres of the Outer Planets Infrared Data Archive. It was recently re-archived (*23*) at https://dataverse.harvard.edu/dataverse/h3p and has the DOI: 10.7910/DVN/KVQWNJ